Journal of Virology®

VIRUS-CELL INTERACTIONS

Contemporary Circulating Enterovirus D68 Strains Infect and Undergo Retrograde Axonal Transport in Spinal Motor Neurons Independent of Sialic Acid

Alison M. Hixon,[a,b] Penny Clarke,[c] Kenneth L. Tyler[c,d,e]

[a]Medical Scientist Training Program, University of Colorado, Aurora, Colorado, USA
[b]Neuroscience Program, University of Colorado, Aurora, Colorado, USA
[c]Department of Neurology, University of Colorado, Aurora, Colorado, USA
[d]Department of Immunology and Microbiology, University of Colorado, Aurora, Colorado, USA
[e]Division of Infectious Disease, Department of Medicine, University of Colorado, Aurora, Colorado, USA

ABSTRACT Enterovirus D68 (EV-D68) is an emerging virus that has been identified as a cause of recent outbreaks of acute flaccid myelitis (AFM), a poliomyelitis-like spinal cord syndrome that can result in permanent paralysis and disability. In experimental mouse models, EV-D68 spreads to, infects, and kills spinal motor neurons following infection by various routes of inoculation. The topography of virus-induced motor neuron loss correlates with the pattern of paralysis. The mechanism(s) by which EV-D68 spreads to target motor neurons remains unclear. We sought to determine the capacity of EV-D68 to spread by the neuronal route and to determine the role of known EV-D68 receptors, sialic acid and intracellular adhesion molecule 5 (ICAM-5), in neuronal infection. To do this, we utilized a microfluidic chamber culture system in which human induced pluripotent stem cell (iPSC) motor neuron cell bodies and axons can be compartmentalized for independent experimental manipulation. We found that EV-D68 can infect motor neurons via their distal axons and spread by retrograde axonal transport to the neuronal cell bodies. Virus was not released from the axons via anterograde axonal transport after infection of the cell bodies. Prototypic strains of EV-D68 depended on sialic acid for axonal infection and transport, while contemporary circulating strains isolated during the 2014 EV-D68 outbreak did not. The pattern of infection did not correspond with the ICAM-5 distribution and expression in either human tissue, the mouse model, or the iPSC motor neurons.

IMPORTANCE Enterovirus D68 (EV-D68) infections are on the rise worldwide. Since 2014, the United States has experienced biennial spikes in EV-D68-associated acute flaccid myelitis (AFM) that have left hundreds of children paralyzed. Much remains to be learned about the pathogenesis of EV-D68 in the central nervous system (CNS). Herein we investigated the mechanisms of EV-D68 CNS invasion through neuronal pathways. A better understanding of EV-D68 infection in experimental models may allow for better prevention and treatment strategies of EV-D68 CNS disease.

KEYWORDS ICAM-5, enterovirus D68, motor neuron, retrograde transport, sialic acid

Enteroviruses (EVs) are among the most prevalent human pathogens. They exhibit a broad range of tissue tropism and cause a wide spectrum of disease (1). While central nervous system (CNS) infection is a relatively rare complication of enterovirus infection, it results in a high degree of morbidity and mortality (2). The most well-known neuropathogenic EVs are the polioviruses (3). However, many nonpoliovirus EVs also cause CNS disease, including enterovirus A71 (EV-A71), enterovirus D70, coxsacki-

Citation Hixon AM, Clarke P, Tyler KL. 2019. Contemporary circulating enterovirus D68 strains infect and undergo retrograde axonal transport in spinal motor neurons independent of sialic acid. J Virol 93:e00578-19. https://doi.org/10.1128/JVI.00578-19.

Editor Terence S. Dermody, University of Pittsburgh School of Medicine

Address correspondence to Kenneth L. Tyler, ken.tyler@ucdenver.edu.

Received 5 April 2019
Accepted 1 June 2019
Accepted manuscript posted online 5 June 2019
Published 30 July 2019

eviruses, and echoviruses, among others (2, 4). The most recent neuropathogenic EV to emerge as a public health concern is enterovirus D68 (EV-D68) (5).

Since 2014, recently evolved lineages of EV-D68, particularly those from subclade B1, have been implicated as a cause of acute flaccid myelitis (AFM), a polio-like paralytic condition that results due to viral infection and injury to the lower motor neurons of the spinal cord (6, 7). Patients present with a viral prodrome typically consisting of fever and upper respiratory symptoms, followed days later by the development of progressive motor weakness with evidence for damage and loss of motor innervation on magnetic resonance imaging (MRI) and electromyography (EMG) (7–10). EV-D68 is predominantly a respiratory pathogen, and the mechanism by which it travels from its initial site of replication in the upper respiratory tract to the spinal cord remains unclear.

Several lines of evidence suggest that viral spread into the CNS via peripheral nerves is an important and conserved mechanism of neuroinvasive enteroviral disease. In 1955, children mistakenly administered an inadequately inactivated batch of poliovirus vaccine developed limb paralysis corresponding to the site of vaccine inoculation (11). Subsequent investigations in transgenic animal models later showed that polioviruses spread into the spinal cord by retrograde axonal transport along motor neuron axons innervating the injected muscle (12, 13). Nerve transection prior to muscle infection prevented poliovirus from spreading to the spinal cord (13). In addition, the highly stereotyped distribution of CNS lesions in cases of fatal EV-A71 brain stem encephalitis suggests that EV-A71 enters the brain stem by infection and retrograde transport along the cranial nerves (14, 15). Experiments in EV-A71 animal models have further supported neuronal spread as a significant mechanism of EV-A71 CNS pathology (16).

We previously developed a neonatal mouse model of EV-D68 infection that recapitulates features of AFM (17, 18). In these mice, infection with contemporary circulating strains of EV-D68 by several routes of inoculation (intracerebral [i.c.], intramuscular [i.m.], or intranasal) induces progressive paralysis due to infection and death of the motor neurons in the spinal cord. Historic strains of EV-D68 do not cause paralysis in this model (17, 19). Examination of strain-specific infection in neuron-like SH-SY5Y cells has suggested that differential receptor utilization patterns may explain the differences in the capacity of circulating and historic EV-D68 strains to infect neurons and cause paralysis (19). Two receptors have recently been identified for EV-D68, sialic acid and intracellular adhesion molecule 5 (ICAM-5) (20, 21). However, the receptor utilization of different EV-D68 strains in motor neurons has not been characterized.

Microfluidic chambers offer a method for analyzing mechanisms of peripheral neuroinvasion (22–24). Neurons can be grown within microfluidic chambers in a way that compartmentalizes the soma and the distal axons, allowing for selective observation or manipulation of either compartment (22, 23). Microfluidic chambers have successfully been used to study axonal transport and the kinetics of alphaherpesviruses (24). In this study, we used human induced pluripotent stem cell (iPSC) motor neurons grown in microfluidic chambers, in addition to the *in vivo* mouse model, to investigate EV-D68 infection and transport at the level of the motor neuron axon. Using a strain of EV-D68 that causes paralytic disease in mice, we show that EV-D68 has the capacity for retrograde, but not anterograde, axonal transport in iPSC motor neurons. Finally, examination of receptor binding showed that contemporary circulating EV-D68 strains do not require the known EV-D68 receptor sialic acid for infection of iPSC motor neuron axons, while historical strains depend on the presence of sialic acid. Furthermore, examination of the distribution and expression of ICAM-5 in the mouse and neuron models suggests that it is not required for motor neuron infection.

RESULTS

Retrograde axonal transport of EV-D68 in the mouse spinal cord. If EV-D68 is neuronally transported from the injected muscle to the motor neurons of the spinal cord, we hypothesized that the motor neurons innervating the injected muscle would be the first cells to show signs of EV-D68 infection. To trace the initial site of spinal cord infection by EV-D68 following i.m. injection, neonatal C57BL/6 mice were infected with

paralytogenic EV-D68 (IL/14-18952 [IL/52]) mixed with tetramethylrhodamine-conjugated dextran (fluoro-ruby), a nontoxic, fluorescent tracer dye (Fig. 1A to D). Littermates were injected in either the right triceps muscle (Fig. 1A), the left triceps muscle (Fig. 1B), the right hamstring muscle (Fig. 1C), or the left hamstring muscle (Fig. 1D). Sectioning and staining of the entire cervical (triceps injected) or lumbar (hamstrings injected) spinal cord segments revealed that fluoro-ruby could be found in the spinal cord corresponding to the injected limb at the spinal cord level associated with the injected muscle as early as day postinfection (dpi) 1, although no viral antigen was detected in any mouse examined at this time point (data not shown). Previous mouse studies have shown that paralysis onset typically occurs on dpi 3 or 4 (17, 18). Examination of the mice at 2 to 3 dpi, prior to the onset of paralysis, revealed that EV-D68 antigen could first be detected in neurons within regions of the cervical and lumbar spinal cord anterior horn regions also containing fluoro-ruby (Fig. 1A to D). These data suggest that the initial site of infection is the motor neurons following retrograde transport of virus by these neurons into the spinal cord from the injected muscle. Examination of a mouse on the day of paralysis onset (dpi 3) revealed significant cell death and loss of the fluoro-ruby-containing cervical spinal cord anterior horn neurons, and EV-D68 antigen could be detected in numerous surrounding cells (Fig. 1E). These results suggest that EV-D68 rapidly spread from the initial site of infection within the anterior horn.

We followed the development of paralysis in an additional litter ($n = 6$) of C57BL/6 mice following i.m. injection of EV-D68 (IL/14-18952). The C56BL/6 mice had the rapid onset of limb paralysis that was identical to the paralysis onset and progression previously seen in Swiss Webster mice (data not shown) (17, 18).

Retrograde axonal transport of EV-D68 in human iPSC motor neurons. We utilized an *in vitro* culture system using fully differentiated human iPSC motor neurons cultured within microfluidic chambers to further investigate the mechanisms of EV-D68 neural spread. These are a highly pure population of iPSCs expressing neuron markers, such as the neuronal cytoskeletal protein neurofilament (NF) and the dendritic marker microtubule-associated protein 2 (MAP2), as well as motor neuron markers, such as choline acetyltransferase (ChAT) (Fig. 2A).

The silicon microfluidic device (Fig. 2B) used in these experiments has two loading wells on each side, which are connected by main channels (Fig. 2C). The main channels are approximately 2,000 μm wide and are connected by ~100 microgrooves that are 450 μm long and 10 μm wide. Due to the considerable hydrostatic pressure within the narrow microgrooves, varying the fluid volume on each side of the device allows for fluidic isolation of one side of the device (e.g., 180 μl somal compared to 130 μl axonal) (22, 23). When cultured in these microfluidic devices coated with Matrigel, which allows neurites to better grip the chamber, these iPSC motor neurons grew in interconnected clusters and extended neurites across the microgrooves (Fig. 2D). Only axonal processes containing the axonal marker NF extended across the microgrooves, while MAP2-positive ($MAP2^+$) dendritic processes could be found only around the motor neuron nuclei (Fig. 2E).

To determine whether EV-D68 could be trafficked by retrograde axonal transport in these iPSC motor neurons, the somal side was isolated by use of a hydrostatic gradient (somal greater than axonal). The axonal side was infected with EV-D68 (IL/14-18952). At 1 h postinfection (hpi), 24 hpi, 48 hpi, and 72 hpi, the neurons and supernatant were collected on the somal side only (Fig. 3A). As expected, the viral titer on the somal side was below the limit of detection at 1 hpi. However, at 24 hpi significant viral growth was detected, and the viral growth further increased by 48 and 72 hpi. Additional axonal infected chambers were collected for viral antigen staining. At 1 hpi, no EV-D68 antigen staining was observed in neurons of the somal side (Fig. 3B). As expected, at 24, EV-D68 antigen was seen in neuron clusters closest to the microgrooves (Fig. 3B). Over 48 and 72 hpi, the number of EV-D68-positive cells increased (Fig. 3B). In addition, the location of EV-D68-infected motor neurons appeared significantly further from the microgrooves over time, which could indicate viral spread between neurons in the

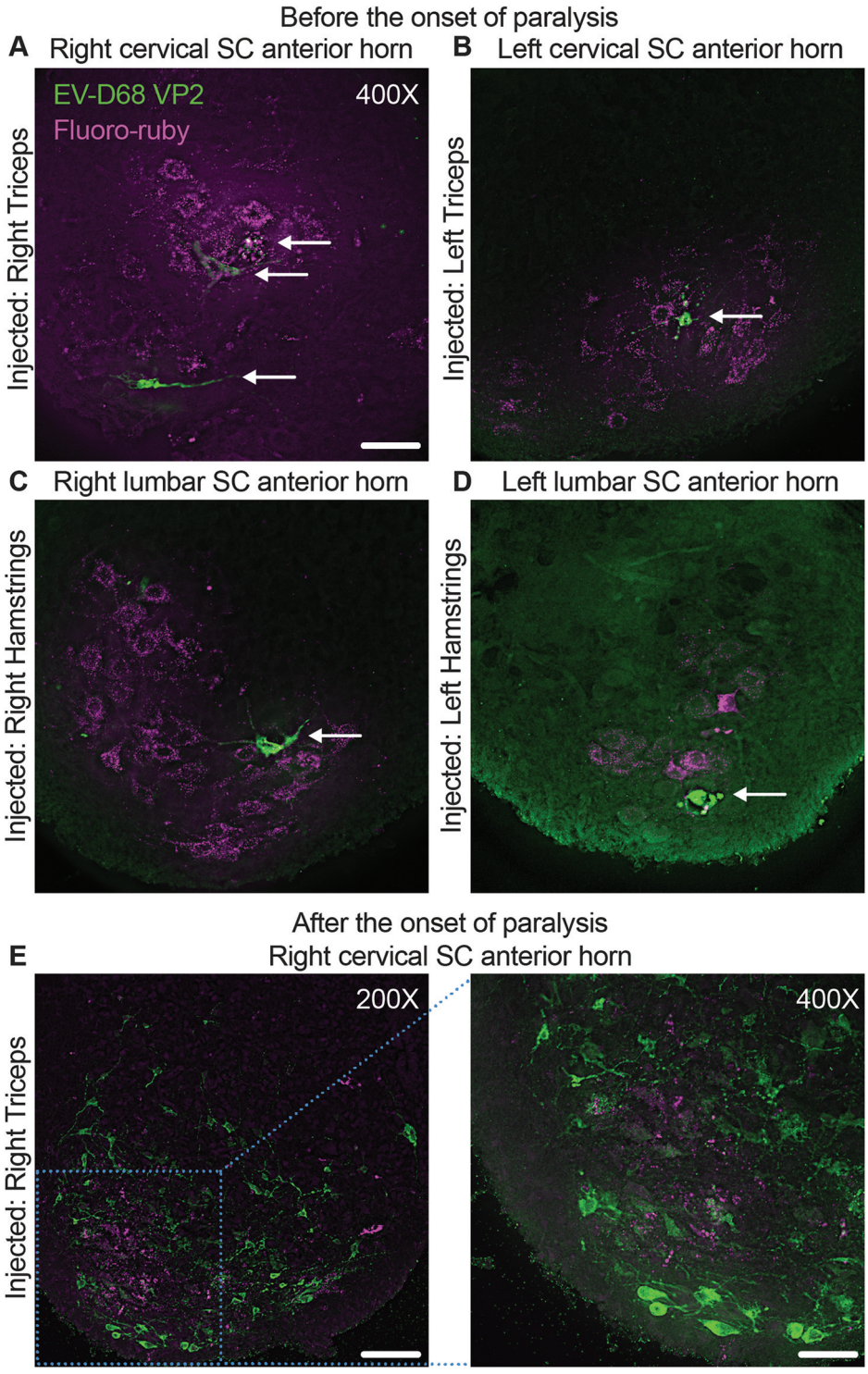

FIG 1 Retrograde axonal transport of EV-D68 in the mouse spinal cord. Mice were coinjected with 10% fluoro-ruby and 1,000 $TCID_{50}$ of EV-D68 IL/14-18952 on postnatal day 2 (P2) of life into either the right triceps (A), left triceps (B), right hamstring (C), or left hamstring (D) muscle and examined for staining of EV-D68 capsid protein VP2 (arrows) before the onset of paralysis on day postinfection (dpi) 2 or 3. The first detectable EV-D68 antigen appeared in motor neurons in the spinal cord (SC) anterior horns corresponding to the injected muscle, as indicated by the presence of fluoro-ruby tracer dye in the right cervical spinal cord anterior horn (A), left cervical spinal cord anterior horn (B), right lumbar spinal cord anterior horn (C), and left lumbar spinal cord anterior horn (D). (E) A mouse injected with 1,000 $TCID_{50}$ EV-D68 IL/14-18952 and 10% fluoro-ruby into the right triceps muscle on P2 began showing signs of moderate paralysis on dpi 3. Images from the cervical spinal cord anterior horn show the death and loss of the fluoro-ruby-expressing neurons and spread of EV-D68 to the surrounding neurons. Bars = 100 μm for the $\times$200-magnification image and 50 μm for the $\times$400-magnification images.

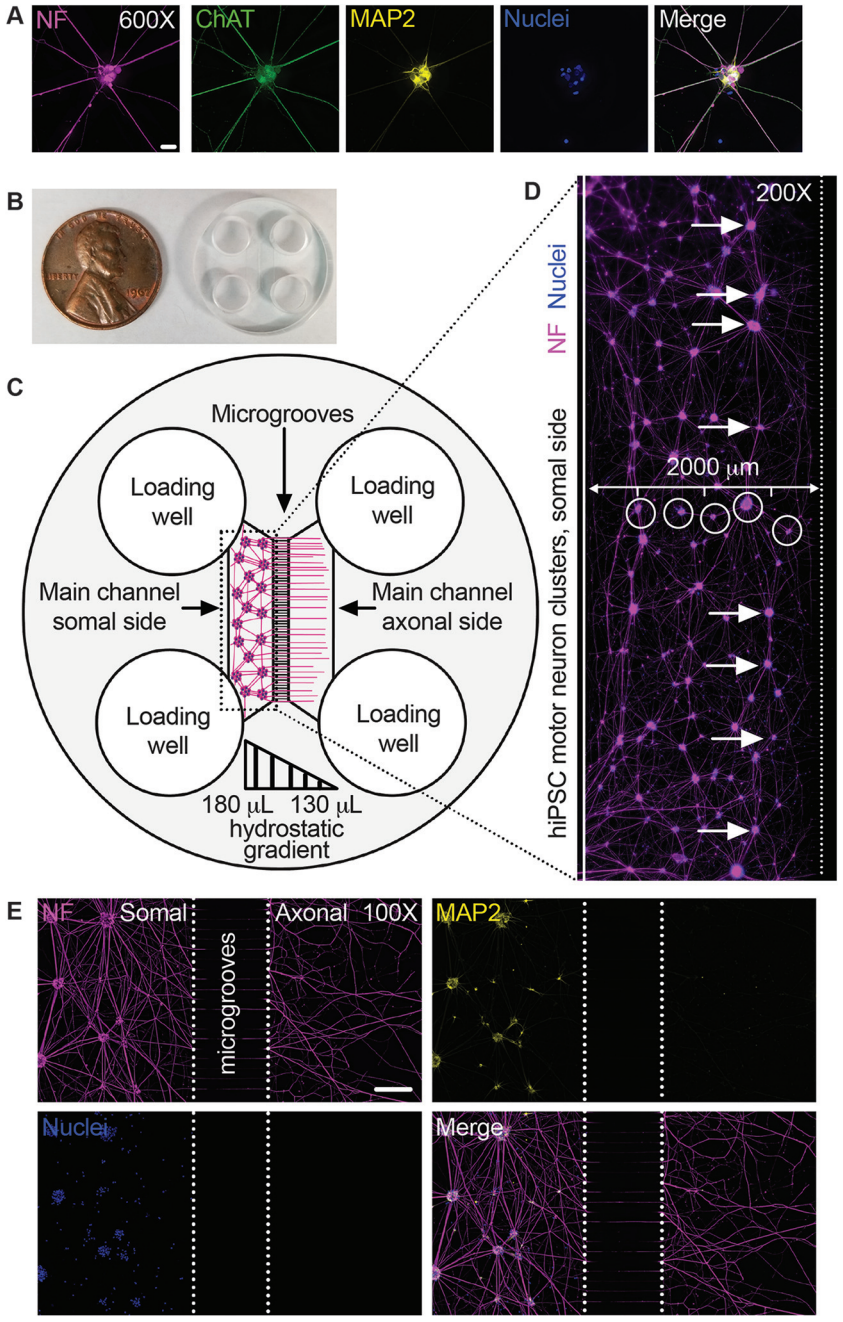

FIG 2 Human iPSC motor neurons cultured in microfluidic chambers. (A) Human induced pluripotent stem cell (iPSC)-derived motor neurons expressed the neuron axon marker neurofilament (NF), the motor neuron protein choline acetyltransferase (ChAT), and neuron dendrite microtubule marker microtubule-associated protein 2 (MAP2). (B) A microfluidic chamber, with a penny used for scale. (C) Schematic of a microfluidic chamber showing each component of the chamber. iPSC motor neurons, drawn as magenta cells with blue nuclei, are shown growing within the main channel of the somal side and extending their axons through 450-μm-long microgrooves to the axonal side main channel. A hydrostatic gradient can be applied to one side of the channel to prevent the flow of fluid from one side to the other. Here the gradient is depicted as 180 μl on the somal side and 130 μl on the axonal side. (D) An extended focal imaging (EFI) scan of the somal side of a microfluidic chamber containing iPSC motor neurons stained for NF and nuclei. The location of the microgrooves is indicated by the dashed line. The location of the back of the main channel is indicated by the solid line. The width of the somal main channel is ~2,000 μm. Neurons clustered at regular intervals from the microgrooves. Neurons in clusters closest to the microgrooves extended their axons across the microgrooves (examples are shown with white arrows). (E) Zooming in on the iPSC motor neurons growing across the microgrooves from the somal side to the axonal side shows that only NF-positive axons cross the microgrooves, while MAP2$^+$ dendrites surround the nuclei. Bars = 200 μm for $\times$100-magnification images and 20 μm for $\times$600-magnification images.

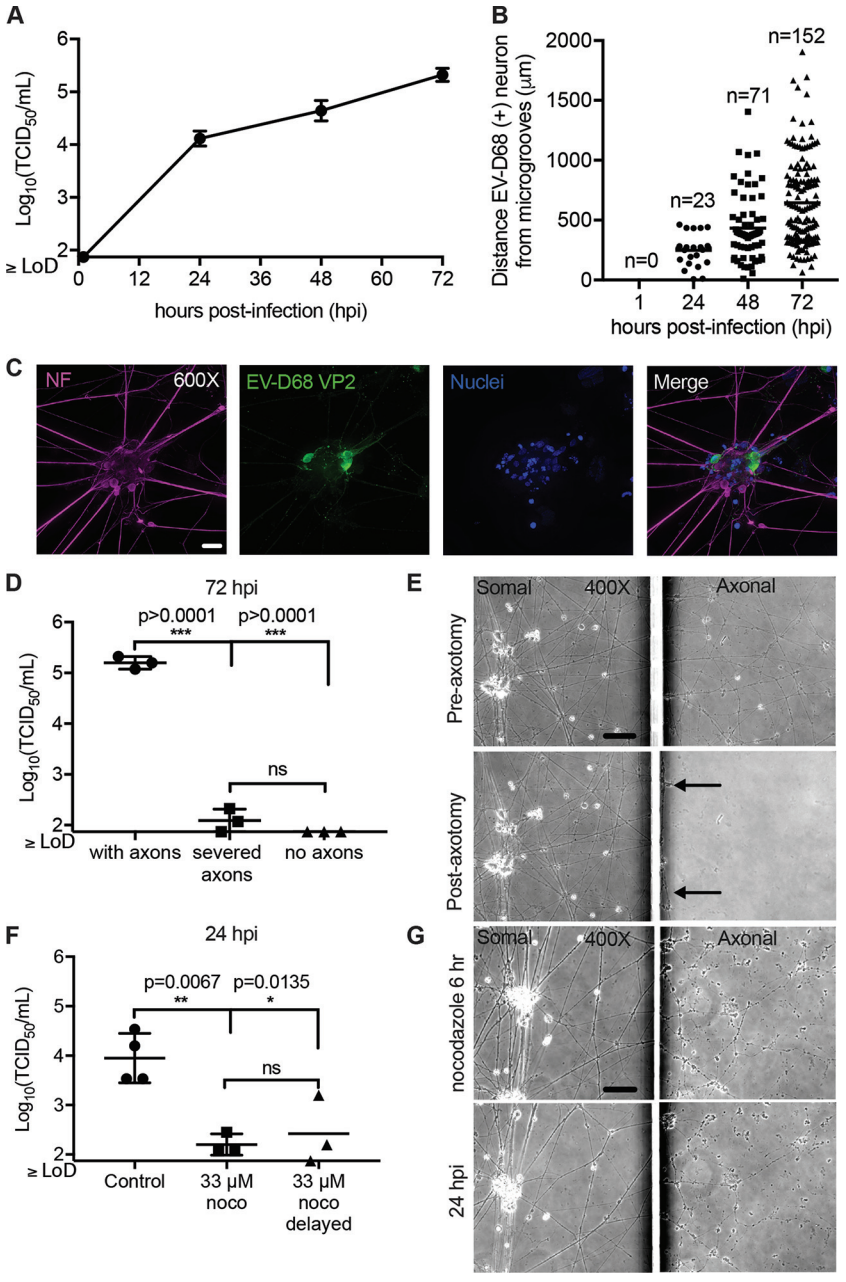

FIG 3 Retrograde axonal transport of EV-D68 in human iPSC motor neurons. (A) iPSC motor neuron axons on the axonal side of the microfluidic chambers were infected with 1×10^5 $TCID_{50}$ of EV-D68 IL/14-18952 for 1 h and then thoroughly rinsed. Chambers ($n = 3$ per time point) were collected a 1, 24, 48, and 72 h postinfection (hpi) and evaluated for viral growth by $TCID_{50}$ assay. (B) Additional chambers ($n = 1$ per time point) were infected on the axonal side as described in the legend to panel A and evaluated for the number of infected neurons and their distance from the microgrooves at 1, 24, 48, and 72 hpi by immunohistochemistry (IHC). No infected neurons were detected at 1 hpi. The number of EV-D68-infected neurons per chamber increased from 24 hpi to 48 hpi and from 48 hpi to 72 hpi, with infected neurons appearing further from the microgrooves over time. (C) Example images of iPSC motor neurons at 48 hpi showing EV-D68 VP2 antigen within their cell bodies and dendrites following axonal infection. (D) Chambers with iPSC motor neuron axons intact ($n = 3$), axons severed by axotomy ($n = 3$), and chambers in which motor neurons were grown in such a way to prevent axons from crossing the microgrooves ($n = 3$) were infected on the axonal side described for panel A and then evaluated for viral growth at 72 hpi. A significant reduction in viral growth was seen in severed axons and under no-axon conditions compared to that for the control with axons, as evaluated by one-way ANOVA followed by Tukey's multiple-comparison test. hiPSC, human iPSC. (E) Phase-contrast images of iPSC motor neurons from chambers pre- and postaxotomy (right images) demonstrate that axotomy did not affect the somal side of the chamber (left images). Black arrows indicate that a few small strands of axon did remain close to the microgrooves after axotomy. (F) Chambers with iPSC motor neurons were treated with the

(Continued on next page)

chamber over time or asynchronous rates of transport to neurons at various distances from the microgrooves (Fig. 3B). An example of a motor neuron cluster with EV-D68-positive motor neurons at 48 hpi is shown in Fig. 3C. EV-D68 antigen staining was localized to the soma and dendrites (Fig. 3C). A cytopathic effect (CPE) was not observed in any chambers over this time period.

Next, we tested whether axons were necessary for the development of infection in the somal compartment. An axotomy was performed on the axonal side of the chamber prior to infection, resulting in the severing of the majority of axons in the axonal compartment (Fig. 3D and E) (22, 23). The axonal side was then infected with virus, and at 72 hpi the somal side was collected for determination of the viral titer (Fig. 3D). Chambers with severed axons had significantly reduced viral titer compared to the controls, with the viral titer being at or below the limit of detection (Fig. 3D). Additional chambers were cultured without Matrigel, and a steep hydrostatic gradient was applied to the chambers during the maturation process (axonal greater than somal). Culturing in this manner prevented axon extension into the axonal side. Virus was applied to the empty axonal side and rinsed after 1 h. After 72 hpi, the somal side was collected for determination of the viral titer. The viral titer was below the limit of detection in all of these chambers (Fig. 3D). Axotomy successfully disrupted the axons of the axonal side but did not affect those on the somal side (Fig. 3E).

Disrupting microtubules has been shown to reduce the axonal transport of other neuroinvasive enteroviruses (16, 25). To test the hypothesis that microtubules are necessary for the retrograde transport of EV-D68, motor neuron axons were exposed to 33 μM nocodazole, a reversible microtubule-depolymerizing drug, for 6 h, starting at 1 h prior to EV-D68 infection (26–28). Nocodazole treatment significantly reduced viral transport in the somal side at 24 hpi compared to that for the controls, as indicated by reduced viral growth (Fig. 3F). These results indicate that microtubules are necessary for axonal transport to the somal side.

Previous studies have shown that 33 μM nocodazole does not affect enterovirus binding, uptake, or RNA release in nonneuronal cells (28). In our experimental system, delaying 33 μM nocodazole treatment until 30 min after the start of EV-D68 infection, by which time EV-D68 should have bound cells and have been taken up by endocytosis, also significantly reduced viral transport to the somal side, as indicated by viral growth, compared to that for the controls by 24 hpi (Fig. 3F). These results indicate that nocodazole treatment did not affect viral binding and entry in neurons (28). While nocodazole treatment caused varicosities and axonal thinning, it did not result in elimination of the axons on the axonal side, and it had no apparent effect on axons or motor neurons in the somal side through the end of the experimental time course at 24 hpi (Fig. 3G).

Absence of anterograde transport of EV-D68 in iPSC motor neurons. To determine if EV-D68 could be trafficked by anterograde transport in iPSC motor neurons, rhabdomyosarcoma (RD) detector cells were seeded in the axonal side of the chamber on the day before infection (24). RD cells are highly susceptible to EV-D68 infection and would be able to replicate virus transported and released in the anterograde direction from the neuron axons, as has been similarly demonstrated in anterograde transport studies with alphaherpesviruses using PK15 detector cells (24). The hydrostatic gradient was established on the axonal side (axonal $\gg$ somal), and the somal side was infected

FIG 3 Legend (Continued)
reversible microtubule toxin nocodazole (noco) ($n = 3$) or the DMSO control ($n = 4$) on the axonal side for 1 h prior to infection, during axonal infection, and for 4 h after infection (6 h total). For one group, nocodazole treatment was delayed until 30 min after the start of viral infection ($n = 3$). A significant reduction in viral titer was seen in the somal side at 24 hpi, as evaluated by one-way ANOVA followed by Tukey's multiple-comparison test. (G) Phase-contrast images of iPSC motor neuron chambers at the end of the 6-h nocodazole treatment and at 24 hpi demonstrate that axons remained in the axonal side (right images) after treatment but showed some thinning and varicosities. Nocodazole did not affect the somal side of the chambers (left images). Bars = 50 μm for the $\times$400-magnification images and 20 μm for the $\times$600-magnification images. LoD, limit of detection.

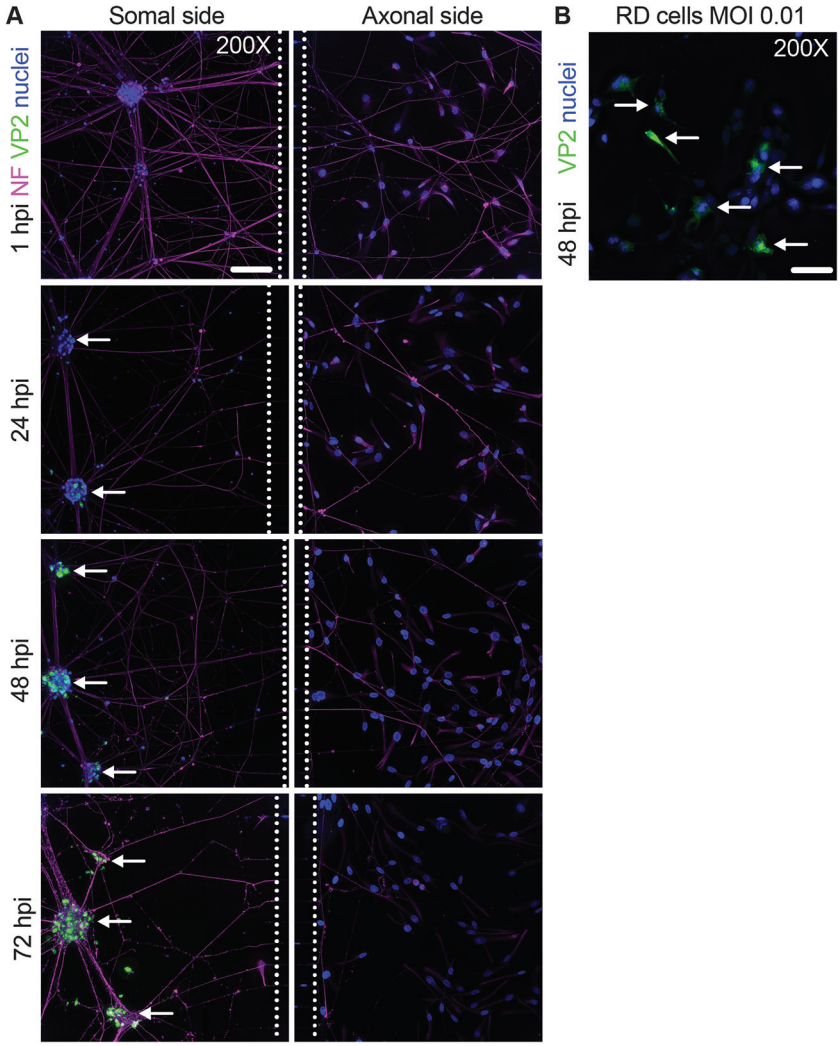

FIG 4 Absence of anterograde transport of EV-D68 in motor neurons. (A) Microfluidic chambers containing iPSC motor neurons were infected on the somal side with 1×10^5 $TCID_{50}$ of EV-D68 IL/14-18952 for 1 h and then thoroughly rinsed. They were then examined for EV-D68 VP2 antigen (green), neurofilament (NF; magenta), and nuclei (blue) in the somal (left) and axonal (right) sides at 1, 24, 48, and 72 h postinfection (hpi). Examples of iPSC motor neuron clusters adjacent to the microfluidic chamber microgrooves (dashed lines) that stained positive for EV-D68 are indicated by white arrows. No EV-D68 antigen was seen in any part of the axonal side at any time point postinfection. (B) Representative images of RD cells infected with EV-D68 IL/14-18952 at an MOI of 0.01 and then examined for EV-D68 VP2 (green, white arrows) and nuclei (blue) at 48 hpi. Images represent the results from three experimental replicates. Note that the neurofilament antibody also produced some staining of the RD cell intermediate filaments. Bars = 100 μm.

with EV-D68 (IL/14-18952). After 1 h, virus was rinsed from the somal side and replaced with normal medium. At 1, 24, 48, and 72 hpi, chambers were collected for viral antigen staining in the somal and axonal sides (Fig. 4A). EV-D68 could be detected in neurons on the somal side at 24 hpi (Fig. 4A). By 48 and 72 hpi, EV-D68 antigen could be found in the majority of neurons within the somal side, including the neurons adjacent to the microgrooves (Fig. 4A). By 72 hpi, neurons on the somal side appeared ragged and had reduced adherence to the chambers during immunostaining compared to that at earlier time points, indicating the start of cell death processes. However, the axonal side RD cells remained healthy and failed to show any signs of a CPE or EV-D68 antigen at any time point (Fig. 4A).

To determine the minimum threshold of sensitivity of the detector cells under the conditions of the chamber, RD cells were cultured in Matrigel and iPSC motor neuron medium with 1% fetal bovine serum (FBS) and were continuously exposed to a multiplicity

of infection (MOI) of 0.01 or an MOI of 0.001 for 48 h. EV-D68 antigen could be readily found in cells infected with an MOI of 0.01 (Fig. 4B) but not those infected with an MOI of 0.001 (data not shown). Given the evidence of robust viral growth by 24 hpi in the motor neurons (Fig. 3A) and the presence of EV-D68 antigen in motor neuron soma by 24 hpi (Fig. 4A), these data indicate that this experimental system should be able to detect RD cell infection following anterograde transport if neurons had released virus at or above a level equivalent to an MOI of 0.01 (50% tissue culture infective dose [$TCID_{50}$], ~100) by 72 hpi. These data indicate that EV-D68 is either not trafficked by anterograde transport in these iPSC motor neurons or trafficked at levels below the limit of detection of this experimental setup.

Contemporary EV-D68 strains do not require sialic acid for infection and axonal transport in iPSC motor neurons. The motor neuron receptor for EV-D68 has yet to be identified. Several previous studies have shown that EV-D68 can bind sialyated glycans, which assist in EV-D68 receptor binding and uncoating (20, 29). However, these studies have also identified sialic acid-independent EV-D68 strains which are capable of binding to sialic acid but do not require it for infection (20, 21). To determine whether EV-D68 requires sialic acid for infection at the level of the iPSC motor neuron axons, we treated axons with neuraminidase (NA), which enzymatically cleaves sialic acid, prior to infection with several different strains of EV-D68, including three contemporary clade B strains from the 2014 EV-D68 outbreak, IL/14-18952 (IL/52), MO/14-18947 (MO/47), and CA/14-4231 (4231). We also tested one clade A strain, USA/N0051U5/2012 (US/TN), which was isolated before the 2014 outbreak, and historic EV-D68 strains Fermon and Rhyne (19). All of the EV-D68 strains tested appeared to be capable of infection and retrograde transport in the human iPSC motor neurons under control conditions (Fig. 5A to F). We found that retrograde axonal transport and infection by IL/52 (Fig. 5A), MO/47 (Fig. 5B), or 4231 (Fig. 5C) were not reduced by NA treatment. In contrast, NA treatment significantly reduced infection by Fermon (Fig. 5D) and Rhyne (Fig. 5E). Even under control conditions, US/TN had a limited ability to infect iPSC motor neurons compared to the other strains, with viral growth in the somal side being near or below the limit of detection (Fig. 5F). After NA treatment, all data points for US/TN were below the limit of detection, although the results for these NA treatment groups were not statistically significantly different from those for the controls. These data support differential receptor utilization between the historic and contemporary EV-D68 strains (19). Contemporary clade B strains (IL/52, MO/47, 4231) can infect and bind to neurons independently of sialic acid, while the clade A strain (US/TN) and prototype strains (Fermon, Rhyne) are sialic acid dependent.

ICAM-5 distribution and expression do not localize to sites of EV-D68 infection. So far, intracellular adhesion molecule 5 (ICAM-5)/telencephalin is the only CNS protein receptor candidate that has been identified for EV-D68 (21). *In vivo* ICAM-5 expression is strictly localized to the neuronal dendrites and cell bodies within the cerebral cortex and olfactory bulbs or telencephalon (30–33). To confirm this pattern of *in vivo* expression, we obtained human brain and spinal cord samples for Western blot analysis. Both adult and pediatric cortical tissue showed strong protein expression for ICAM-5 at a size of approximately 130 kDa (Fig. 6A). In contrast, pediatric cervical spinal cord tissue showed a complete absence of ICAM-5 protein expression (Fig. 6A). These data fail to support a pattern of ICAM-5 expression that would suggest it to be an important receptor for EV-D68 within the human spinal cord.

We next investigated ICAM-5 RNA and protein expression in the *in vivo* mouse model of EV-D68 infection (Fig. 6B and C). In postnatal day 2 (P2; the typical day of i.m. and i.c. infection) mice, we detected very low levels of ICAM-5 RNA in the brain and spinal cord compared to the levels seen in the adult mouse cortex (the positive control) (Fig. 6B). Previous studies have shown that ICAM-5 may be an important signaling molecule for immune cell regulation during viral CNS infection; therefore, we also examined ICAM-5 expression at 6 days postinfection (dpi) i.m. with EV-D68 strain IL/14-18952 or mock-infected controls (34, 35). ICAM-5 RNA expression was slightly higher in both infected and mock-infected mouse brains than in the P2 mouse brains;

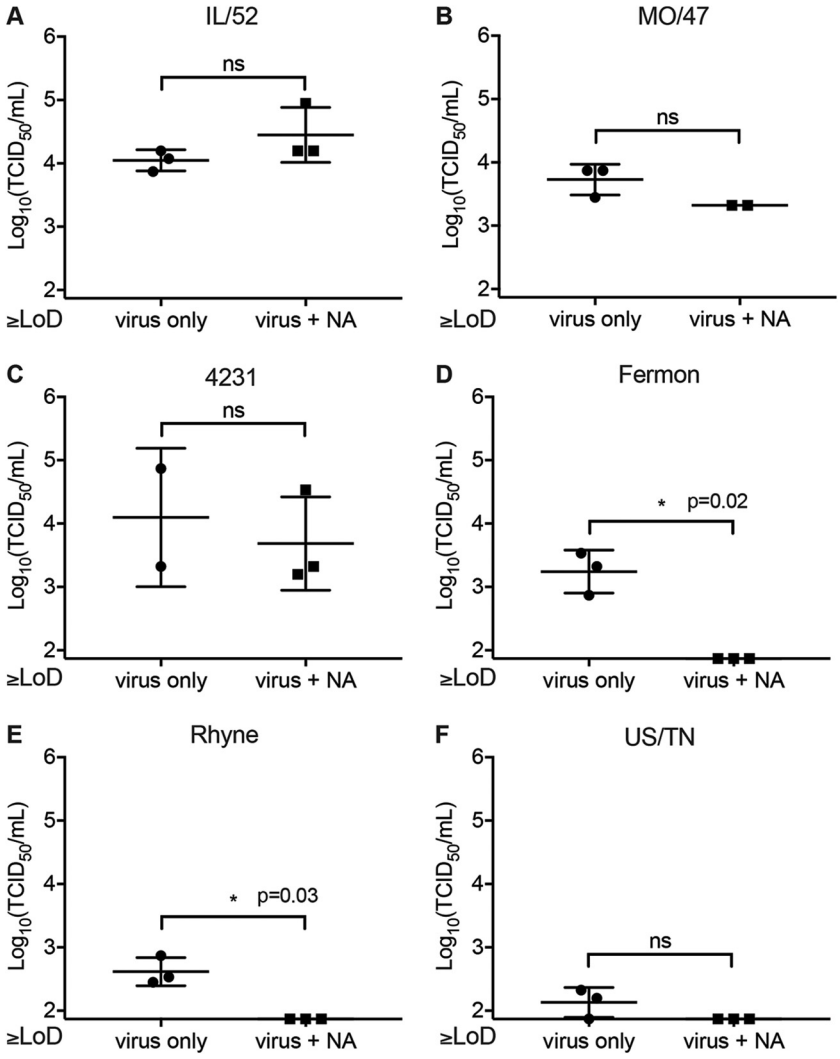

FIG 5 Characterization of sialic acid-mediated infection in iPSC motor neurons. Microfluidic chambers ($n = 2$ to 3 per experimental condition) containing iPSC motor neurons were treated with 100 mU/ml of neuraminidase on the axonal side for 1 h, followed by infection for 1 h with 1×10^5 $TCID_{50}$ of EV-D68 IL/14-18952 (IL/52) (A), MO/14-18947 (MO/47) (B), CA/14-4231 (4231) (C), Fermon (D), Rhyne (E), or USA/N0051U5/2012 (US/TN) (F). Differences between the controls and the neuraminidase-treated groups were evaluated by Welch's *t* test. ns, not significant.

however, ICAM-5 RNA expression was still ~5-fold lower than that in the adult mouse cortex (Fig. 6B). ICAM-5 expression did not differ significantly between infected mice and uninfected controls in either the brain or the spinal cord, indicating that the increase of ICAM-5 in these animals was due to normal developmental expression. The ICAM-5 protein was not expressed in the P2 mouse brain and was expressed at low levels in both uninfected and EV-D68-infected mice by dpi 6 compared to the level in the cortex of the adult controls at a size of approximately 130 kDa (Fig. 6C). The ICAM-5 protein was not detected in the spinal cord of any mouse examined (Fig. 6C). ICAM-5 was also not detected in mouse muscle by PCR or Western blotting at P2 or in dpi 6 controls and infected mice (data not shown). These data suggest that ICAM-5 is unlikely to play a role in EV-D68 infection of mouse motor neurons *in vivo* following i.m. or i.c. infection at P2, as its developmental distribution and expression do not correlate with the known localization of viral growth and cellular injury.

To investigate whether ICAM5 plays a role in EV-D68 infection of motor neurons *in vitro*, we next performed Western blot assays for ICAM-5 on whole iPSC motor neuron lysates. HeLa and RD cell positive-control lysates had strong protein expression of a

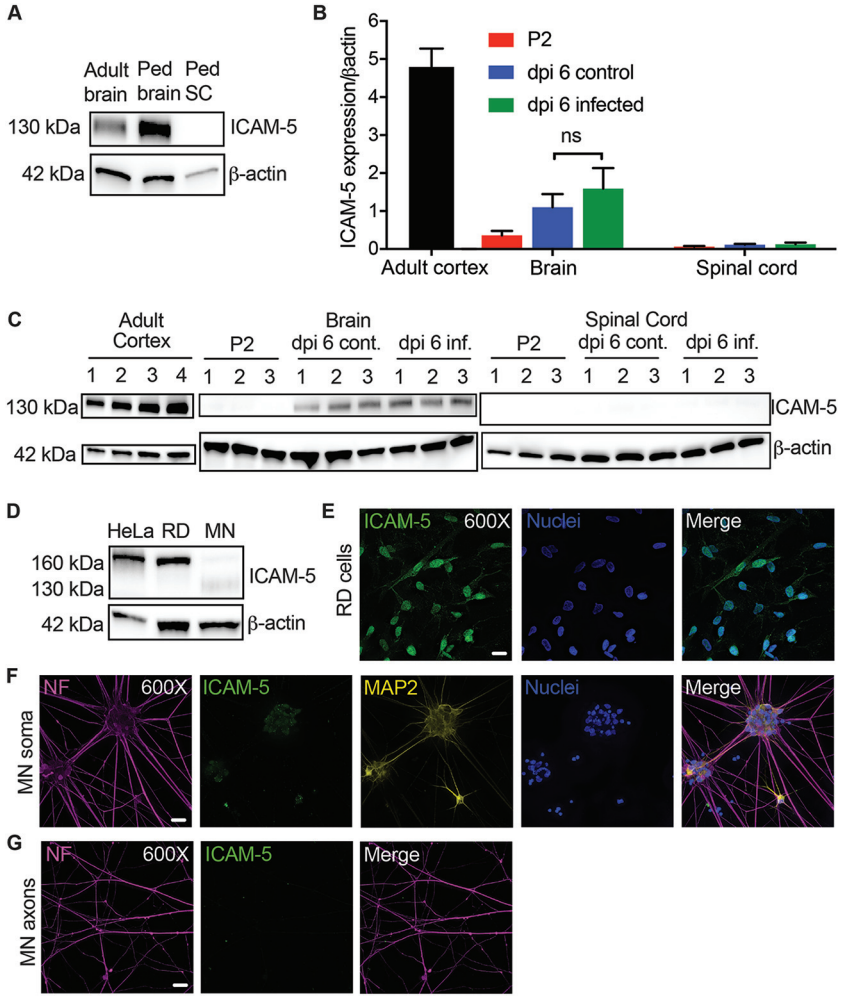

FIG 6 Characterization of ICAM-5 expression in humans, mice, and motor neurons. (A) ICAM-5 expression by Western blotting (WB) in the human adult temporal cortex (adult brain) compared to expression in the pediatric (Ped) frontal cortex (Ped brain) and cervical spinal cord (Ped SC) from a 3-year-old human child. ICAM-5 was not detected in the pediatric cervical spinal cord. All samples contained 10 μg of total protein. (B) Neonatal mice were evaluated for ICAM-5 RNA expression normalized to β-actin expression by RT-qPCR on P2 (the standard age of injection; $n = 3$) as well as on dpi 6 following i.m. injection of 1,000 $TCID_{50}$ of EV-D68 IL/14-18952 ($n = 3$) or the control used for mock injection ($n = 3$). Cortical tissue from 8-week-old mice ($n = 4$) was used as a positive control. There was no significant difference between ICAM-5 RNA expression on day postinfection 6 for the control and EV-D68-injected mouse brains ($P = 0.5386$), as evaluated by one-way ANOVA between all groups followed by Tukey's multiple-comparison test. (C) ICAM-5 expression by Western blotting mirrored the findings of RT-qPCR in the adult mouse cortex ($n = 4$) as well as P2 ($n = 3$), dpi 6 infected ($n = 3$), and dpi 6 control (cont; $n = 3$) brains and spinal cords. All samples contained 20 μg of total protein. (D) ICAM-5 protein expression in RD and HeLa cells and iPSC motor neurons (MN) by Western blotting. All samples contained 20 μg of total protein. (E) The strong ICAM-5 protein expression seen in RD cells was confirmed by immunohistochemistry (IHC). (F and G) Faint, punctate ICAM-5 staining was observed in the iPSC motor neuron soma and dendrites (F) by IHC but not in the axons (G). Images represent results from three experimental replicates. Bars = 20 μm.

160-kDa isoform of ICAM-5, while low levels of two ICAM-5 isoforms (sizes of approximately 160 kDa and 130 kDa) were seen in motor neuron lysates (Fig. 6D). RD cells stained for ICAM-5 showed expression of ICAM5 throughout their cell surfaces and nuclei (Fig. 6E). In contrast, immunohistochemistry (IHC) demonstrated that ICAM-5 was limited to faint punctate staining around the iPSC motor neuron soma and dendrites (Fig. 6F) but was not expressed on the iPSC motor neuron axons (Fig. 6G). These data correlate with the known expression of ICAM-5 as a somatodendritic, but not axonal, adhesion molecule (30, 33). Due to a lack of expression on the axon, ICAM-5 is unlikely

to play a role in axonal infection and retrograde transport for sialic acid-independent EV-D68 strains, as only axons cross the microgrooves, as previously shown in Fig. 2E.

DISCUSSION

Here we used *in vivo* and *in vitro* models to investigate neuroinvasion by EV-D68. We found that retrograde axonal transport is a major mechanism of EV-D68 CNS infection. *In vivo* and *in vitro*, paralytic EV-D68 strain IL/14-18952 is taken up by motor neuron axons and then travels along the axon microtubules to the soma. In mice, viral antigen appears in the anterior horn of the spinal cord within 48 h of i.m. infection. To do this, virus must first replicate in the muscle, be taken up by the motor neuron, be transported within the innervating axon, and replicate within the neuron. The speed of this process is more consistent with fast retrograde axonal transport (200 to 400 mm/day) than slow axonal transport (0.1 to 8 mm/day) (36). In the microfluidic chambers, virus must travel at least 450 μm through the microgrooves to get to the neuron soma. The detection of $\sim 10^4$ $TCID_{50}$/ml of viral growth within 24 h of axonal infection and transport is, again, more consistent with high rather than low rates of axonal transport. Drug treatment with the microtubule toxin nocodazole significantly reduced the amount of virus transported to the soma, further supporting the utilization of a known mechanism of retrograde transport along microtubules by EV-D68 virions.

We found no evidence for the anterograde transport and release of EV-D68 from axons following infection and replication in the soma of iPSC motor neurons. To examine this, we used an experimental setup similar to that utilized to study anterograde transport of pseudorabies virus strains from neurons to detector cells within 24 h postinfection (24). Fast retrograde transport requires the molecular motor dynein, which always moves cargo toward the nucleus of the cell (37). Fast anterograde transport utilizes the motor protein kinesin, which always transports cargo away from the nucleus (37). These data suggest that EV-D68 may preferentially bind to retrograde motor proteins, as has been described with poliovirus and the dynein light chain protein Tctex-1 (38). However, as we investigated only one type of neuron in these studies, we cannot rule out the possibility of multidirectional transport of EV-D68 in other types of neurons.

The preference for retrograde rather than anterograde transport fits with previous observations in our mouse model. During development of the mouse model, we found that paralytogenic EV-D68 strains MO/14-18947 and IL/14-18952 produce disease in mice at a higher frequency following i.m. infection than following i.c. infection, dependent on the viral strain and the titer of the injected inoculum (17, 18). These observations are in contrast to those with other neurotropic viruses, such as reovirus and West Nile virus, in which disease is more easily produced by direct CNS infection rather than peripheral infection (39, 40). These differences between viruses may be explained by a combination of tissue tropism and neuroanatomy. EV-D68 appears to have strong *in vivo* tropism for motor neurons, as opposed to neurons in general. Human AFM patients present with inflammation and the loss of motor neurons in the brain stem and spinal cord but do not show signs of generalized encephalitis (7, 10). Consistent with this observation, studies with mouse models developed by several independent research groups have shown that infection by contemporary EV-D68 strains results in minimal replication within the brains of infected animals but robust replication in spinal cord and muscle tissue (17, 41, 42). In addition, motor pathways from the upper motor neurons of the brain to the lower motor neurons are anterograde connections. The nature of these neuroanatomical pathways suggests that EV-D68 injected within the brain would spread less efficiently due to its preference for retrograde transport. Other possible indirect pathways to the spinal cord motor neurons include transport via anterograde sensory and cerebellar connections or retrograde transport into the spinal cord from muscle infection following viremia.

We have previously shown that the pattern of limb paralysis following i.m. injection into the left hind limb is highly stereotyped, beginning in the injected limb followed by the contralateral hind limb and then the ipsilateral forelimb (17, 18). The spinal cord

contains complex, hierarchical networks of neurons and interneurons that participate in the production of patterned limb movement (43). The observations in the mouse model could be consistent with rapid neural spread between these networks of spinal cord neurons through either the release of virions by cell lysis or active transport between neurons. In the microfluidic chambers, viruses also appear to spread to increasing numbers of iPSC motor neurons further distances from the microgrooves following axonal infection. Further studies need to be performed to determine the exact pathways and mechanisms of EV-D68 spread between neurons *in vivo* and *in vitro*. Of note, while neurons undergo rapid death *in vivo* within 3 days following i.m. inoculation, a cytopathic effect was not observed in the iPSC motor neuron cultures following retrograde axonal transport. It is unclear why the iPSC cultures exhibited less cell death, but resistance to virus-induced cell death has been noted in other studies using neuron cultures (44–46). It is possible that the iPSCs expressed more inhibitors of apoptosis (45) or that the iPSCs expressed lower levels of an EV-D68 receptor(s) than *in vivo* motor neurons (46). Another possibility is that components of the innate immune response, such as microglia, which are not present *in vitro*, contribute to neuron cell death *in vivo*.

The microfluidic chamber model also allowed us to investigate putative motor neuron receptor candidates involved in neuronal infection and spread. Clade B strains were the most widely circulating strains detected during the 2014 EV-D68 outbreak (47). Clade B lineage strains, particularly clade B1, have been the EV-D68 strains most frequently isolated from AFM patients (48, 49). Recent work has shown that neuron-like SH-SY5Y cells are susceptible to infection by contemporary circulating EV-D68 strains from the 2014 outbreak, including those from clade B (IL/14-18952, MO/14-18947, CA/14-4231), but not older stains (Fermon, Rhyne) or the 2012 clade A strain US/TN (19). The susceptibility of SH-SY5Y cells to these contemporary circulating strains but not to the other strains correlated with receptor binding efficiency, as examined by virus binding assays (19).

Two uncoating receptors have been identified for EV-D68, sialic acid and ICAM-5 (20, 21, 29). These studies have shown that some strains of EV-D68 require the cell surface expression of specific forms of sialic acid for infection, while other strains infect in a sialic acid-independent manner (20, 21, 29). ICAM-5 expression is limited to dendrites of the telencephalon, a location in which EV-D68 infection is never seen in humans or in animal models, yet transfection of this protein in unsusceptible cell lines confers susceptibility to EV-D68 infection (21). Even when ICAM-5 is expressed, older EV-D68 strains (Fermon) still require the presence of sialic acid on ICAM-5 for infection (21). We first explored the role of sialic acid in axonal infection. In contrast to SH-SY5Y cells, human motor neurons were universally susceptible to infection, retrograde axonal transport, and viral growth by all of the EV-D68 strains tested. However, cleavage of sialic acid completely inhibited axonal infection and viral growth by the older EV-D68 strains (Fermon, Rhyne) and US/TN, whereas it had no effect on infection by the contemporary circulating strains. These groupings corresponded to the susceptibility to infection and receptor binding described in the previous experiments with SH-SY5Y cells (19). Examination of the SH-SY5Y transcriptome by RNA sequencing (RNA-seq) showed that the SH-SY5Y cells used in these experiments had no detectable transcription of sialic acid linkage enzymes *ST3GAL4* and *ST6GAL1* (D. M. Brown, personal communication) (19). It has been found that double knockout of these enzymes significantly reduces sialic acid-dependent EV-D68 infection (20). These data indicate that the differences in receptor binding and infection found between contemporary and older EV-D68 strains in the SH-SY5Y cell experiments could be explained by a lack of these specific linkages of sialic acid on the surface of these cells. These findings further support a model of altered tropism in contemporary EV-D68 strains compared to older strains. In neurons and neuron-like cells, infection by contemporary EV-D68 strains from the 2014 outbreak appears to be sialic acid independent.

Our ICAM-5 studies suggest that ICAM-5 cannot be the receptor utilized by EV-D68 in human children, mice, or motor neuron axons. Furthermore, ICAM-5 transcription

was not detected in SH-SY5Y cells, as indicated by RNA-seq (D. M. Brown, personal communication) (19). One limitation to these studies is that they were only observational, as tools to specifically block the binding site of EV-D68 on ICAM-5, such as a monoclonal antibody, are not currently available, to our knowledge. Nevertheless, the identification of ICAM-5 may prove to be an important step in the discovery of additional EV-D68 neuronal receptors. Recent attempts to cocrystallize EV-D68 bound to ICAM-5 have been unsuccessful, consistent with a very low binding affinity of EV-D68 to ICAM-5 (50). ICAM-5 is a member of the immunoglobulin superfamily of proteins, and the majority of enteroviruses utilize this family of protein receptors for infection in various tissues (51). EV-D68-targeted tissues may contain immunoglobulin family proteins with moieties similar to ICAM-5 that serve as binding partners to EV-D68, and identification of these moieties could be used to screen for additional receptor candidates.

MATERIALS AND METHODS

Cell lines. Rhabdomyosarcoma (RD) and HeLa cells were obtained from ATCC and maintained in vapor-phase liquid nitrogen until use. RD and HeLa cells were cultured in high-glucose Dulbecco's modified Eagle medium (DMEM) with L-glutamine and sodium pyruvate (catalog number 6429; Sigma-Aldrich) with 10% FBS. iCell motor neurons (catalog number R1051), a line of fully differentiated human-induced pluripotent spinal motor neurons, were obtained from Fujifilm Cellular Dynamics (Madison, WI) and stored and cultured according to the manufacturer's protocols.

Viral stocks and titers. EV-D68 strains IL/14-18952 (clade B2, GenBank accession no. KM851230) and MO/14-18947 (clade B1, GenBank accession no. KM851225) were obtained from ATCC; strains Fermon (prototype strain, GenBank accession no. KU844179), Rhyne (prototype strain, GenBank accession no. KU844178), and CA/14-4231 (clade B2, GenBank accession no. KU844181) were obtained from Shigeo Yagi at the California Department of Public Health; and strain USA/N0051U5/2012 (clade A, GenBank accession no. KT347280) was obtained from Tina Hartert at Vanderbilt University (19). Viral stocks were inoculated onto flasks containing ~80% confluent RD cells and grown at 33°C until the cells were dead or dying. The cells were then lysed by three freeze-thaw cycles. Cell lysates were spun at 141,000 × *g* in an ultracentrifuge using a Beckman Coulter SW41 Ti rotor for 30 min at room temperature to remove cell debris. Virus was then pelleted from the supernatant through a 20% sucrose cushion at 141,000 × *g* in the ultracentrifuge using a Beckman Coulter SW28 rotor overnight (14 to 16 h) at room temperature. Viral pellets were resuspended in sterile phosphate-buffered saline (PBS) and stored at −80°C.

Viral titers were determined using a standard 50% tissue culture infective dose ($TCID_{50}$) assay in RD cells in 96-well plates. Tenfold dilutions were made using standard DMEM with 100 U/ml penicillin-streptomycin. Assay plates were incubated at 33°C for 2 weeks, and then the viral titer (in numbers of $TCID_{50}$ per milliliter) was determined by the Kärber method.

Human tissue. Deidentified, postmortem human pediatric frontal cortex and cervical spinal cord tissues were obtained with permission from the Children's Hospital Colorado Pathology Department. The tissue was acquired from the autopsy of a 3-year-old male child who died due to a brain tumor. Deidentified human adult temporal cortical tissue was obtained with permission from the University of Colorado Denver Central Nervous System Biorepository under a study use agreement (COMIRB 13-3007). This tissue was collected from an adult patient undergoing surgical resection for temporal lobe epilepsy. All tissue was stored at −80°C.

Mouse experiments. All mice were maintained in an Association for Assessment and Accreditation of Laboratory Animal Care (AAALAC)-accredited animal facility at the University of Colorado. Untimed pregnant C57BL/6 females were ordered from Envigo and maintained in a standard animal facility prior to the birth of the pups. Additional C57BL/6 pups were produced by pair breeding within the animal facility. All experiments were approved by the Institutional Animal Care and Use Committee (IACUC) under protocol number B-34716 (03) 1E. Animals were anaesthetized with inhaled isoflurane until they were areflexic prior to endpoint tissue collection.

Mouse injections. Pups were injected on postnatal day 2 (P2) of life. Pups received 1,000 $TCID_{50}$ of viral stock in PBS or PBS alone as a control by intramuscular (i.m.) injection via tuberculin syringe (10-μl total volume). For viral retrograde tracer experiments, pups ($n = 6$ to 8 per litter) received 1,000 $TCID_{50}$ virus plus 10% 10,000-molecular-weight (MW) tetramethylrhodamine-dextran fluoro-ruby (catalog number D1817; Thermo Fisher) in 10 μl of PBS. The pups were monitored daily for signs of paralysis. Paralysis was scored using a motor impairment score as previously described (18). Briefly, pups were placed on a flat surface and observed for limb movements. Each limb was then scored, with a score of 0 indicating no impairment, a score of 1 indicating slight impairment, a score of 2 indicating moderate impairment, and a score of 3 indicating severe impairment. The final score was calculated by summing the score for each limb. Pups that failed to gain weight or appeared lethargic were euthanized.

Microfluidic chambers. Sterilized Xona microfluidic chambers (catalog number RD450) were adhered to poly-D-lysine (PDL)-treated 50-mm Ibidi μ-dishes (catalog number 81136) according to the manufacturer's instructions. A 2% Matrigel (catalog number 356234; Corning) solution was added to one side of the microfluidic chamber and allowed to completely coat the microgrooves at 37°C overnight. On the next day, the other side of the chamber was coated with 2% Matrigel at 37°C for 1 h. The Matrigel was removed, and motor neuron medium was added to the chambers. The motor neurons were thawed and reconstituted in motor neuron medium according to the manufacturer's protocol. In order to achieve

a density suitable for plating within the microfluidic chambers, the motor neurons were pelleted by centrifugation at 300 × *g* for 20 min and resuspended in approximately 0.5 ml of medium. The motor neurons were added to the somal side at a density of 50,000 cells per chamber. The motor neurons were allowed to settle within the main channel for 30 min at room temperature, and then up to 130 μl motor neuron medium was added to the somal side. The axonal side was kept at a higher volume than the somal side for 72 h to prevent the motor neurons from flowing into the microgrooves prior to adherence, after which the volumes between the somal and axonal sides of the chamber were kept equal. The medium was changed at 24 h after plating and then changed every 48 to 72 h. Neurons were allowed to mature and extend their axons across the microgrooves for 2 weeks (days *in vitro* [DIV] 13 to 15) prior to experimental use.

For all axonal infection experiments, the somal side of the chamber was hydrostatically isolated with 180 μl of medium (somal greater than axonal). Virus was added to the axonal side at 1×10^5 $TCID_{50}$ in 130 μl of medium. Virus was incubated on the axons for 1 h at 37°C. Virus was then aspirated from the loading wells, and the main channel was rinsed with 65 μl of PBS through each loading well three times, for a total of six rinses of the axon main channel. After rinsing, 130 μl of normal motor neuron medium was replaced on the axonal side.

For axotomy, medium was aspirated from the loading wells until a bubble of air was passed through the axon main channel (22). The procedure was repeated three times or until the majority of axons were severed.

For nocodazole treatment, the somal side was hydrostatically isolated and 33 μM nocodazole (or the dimethyl sulfoxide [DMSO] control) in 130 μl motor neuron medium was added to the axonal side for 1 h at 37°C. The pretreatment was aspirated, and 1×10^5 $TCID_{50}$ virus with 33 μM nocodazole in 130 μl was added to the axonal side for 1 h. Virus was then rinsed six times with PBS containing 33 μM nocodazole, and 130 μl of medium containing 33 μM nocodazole was added for 4 h at 37°C, for a total of 6 h of nocodazole treatment. Nocodazole was aspirated, and the axonal side was rinsed six times with PBS and allowed to recover in motor neuron medium for the duration of the experiment. For delayed nocodazole treatment, 1×10^5 $TCID_{50}$ of virus was added to the axonal side for 30 min and then replaced with 1×10^5 $TCID_{50}$ of virus and 33 μl nocodazole for 30 min. Virus was then rinsed six times with PBS containing 33 μM nocodazole, and 130 μl of medium containing 33 μM nocodazole was added for 5.5 h at 37°C, for a total of 6 h of nocodazole treatment. Nocodazole was aspirated, and the axonal side was rinsed six times with PBS and allowed to recover in motor neuron medium for the duration of the experiment.

For anterograde transport, RD cells in motor neuron medium supplemented with 1% FBS were added to the axonal side on the day before infection at a density of 5,000 cells per chamber (24). The axonal side was hydrostatically isolated with 180 μl of motor neuron medium with 1% FBS (axonal greater than somal). Virus was added to the somal side at 1×10^5 $TCID_{50}$ in 130 μl for 1 h at 37°C. Virus was removed from the loading wells, and the main channel was gently rinsed with 65 μl of PBS through each loading well three times, for a total of six rinses. After rinsing, 130 μl of normal motor neuron medium was replaced on the somal side.

For neuraminidase (catalog number 2876; Sigma-Aldrich) treatment, the somal side was hydrostatically isolated and 100 mU/ml neuraminidase in motor neuron medium was added to the axonal side for 1 h at 37°C (29). The neuraminidase was then aspirated from the axonal side, and the main channel was rinsed once with PBS, prior to virus infection as described above (29).

Fluorescent IHC. Neonatal mouse spinal cords were fixed in periodate-lysine-paraformaldehyde (PLP) fixative overnight at 4°C (17). The spinal cords were dehydrated in 30% sucrose–PBS until they were saturated. The tissue was then conditioned to the freezing medium by incubating it in 1:1 20% sucrose–PBS and OCT overnight at 4°C. The spinal cords were sectioned into cervical, thoracic, and lumbar regions, positioned within an embedding mold containing OCT, and flash frozen in liquid nitrogen. Spinal cord sections were cut on a −20°C Leica cryostat at 20 μm per slice in a continuous series. The slides were dried overnight and then stored at −20°C until staining. For staining, slides were warmed to room temperature and rehydrated in PBS. Tissue sections were permeabilized in 0.3% Triton X-100 in PBS (PBSX) for 30 min and then blocked in 5% normal serum in PBSX for 1 h. Tissue was incubated in primary antibodies overnight at 4°C. After three rinses in PBS, the slides were then incubated in secondary antibody in blocking solution (PBSX and 5% normal serum) for 1 h at room temperature. The slides were washed in PBS three times and rinsed with water, and then a coverslip was placed with Prolong Diamond antifade mountant (catalog number P36965; Invitrogen).

For microfluidic chambers, all immunohistochemistry (IHC) steps were performed within the chambers. RD cells were cultured for staining in either 35-mm Ibidi culture dishes (catalog number 80136). Cultures were rinsed once in ice-cold phosphate-buffered saline containing calcium and magnesium (PBS+/+). The cells were fixed in PLP for 30 min on ice. The cells were rinsed three times in PBS+/+ and permeabilized for 5 min in 0.03% Triton-X in PBS+/+. The cells were rinsed three times in PBS+/+ and blocked in 5% normal serum in PBS+/+ for 1 h at room temperature. The cells were then incubated in primary antibodies in the blocking solution overnight at 4°C. Following primary incubation, the cells were rinsed three times in PBS+/+ and incubated with secondary antibodies in blocking solution for 1 h at room temperature. Secondary antibodies were removed by rinsing three times in PBS+/+. Nuclei were then stained by adding 10 ng/ml Hoechst 33342 stain (catalog number H3570; Invitrogen) in distilled H_2O. The Hoechst stain was removed by rinsing three times with PBS+/+ and once with water. Stained cultures were covered in mounting medium, and a coverslip was placed on top. Chambers were maintained in sterile H_2O following staining, and the culture dishes were wrapped in Parafilm to prevent drying.

The following primary antibodies were used: rabbit anti-EV-D68 VP2 (catalog number GTX132314; GeneTex), rabbit anti-ChAT (catalog number ab178850; Abcam), chicken anti-NF (1:500; catalog number CH22104; Neuromics), mouse anti-MAP2 (catalog number ab11267; Abcam), and rabbit anti-ICAM-5 (catalog number ab192415; Abcam). All of the following Alexa Fluor (Invitrogen) secondary antibodies were used at a 1:1,000 concentration: goat anti-rabbit immunoglobulin-Alexa Fluor 488 (catalog number A11034), goat anti-rabbit immunoglobulin-Alexa Fluor 647 (catalog number 27040), goat anti-mouse immunoglobulin-Alexa Fluor 488 (catalog number 28175), goat anti-mouse immunoglobulin-Alexa Fluor 633 (catalog number 21052), and goat anti-chicken immunoglobulin-Alexa Fluor 568 (catalog number 11041).

All samples were imaged on an Olympus IX83 light microscope with cellSens imaging software. Chambers stained, evaluated for the number of infected neurons, and the distance of the infected neurons from the microgroove were imaged across the entire somal main channel as a single plane at a magnification of ×200. Neuron distance was measured linearly from the closest edge of the microgrooves to the center of the neuron nucleus using Olympus cellSens software. Immunofluorescent images taken for publication were imaged as a z-series and processed using advanced maximum likelihood constrained iterative deconvolution (52). In-focus planes were extracted and combined in a maximum z-stack projection for the final image. Images were brightened linearly and equally in the Fiji platform (53).

Western blotting. For neonatal mice, whole brains with olfactory bulbs, whole spinal cords, and muscle tissue from the injected limb were dissected into Benchmark Bead Bug collection tubes (catalog number 1032-30) and flash frozen in liquid nitrogen. For adult cortex samples, brains were removed from 8-week-old male C57BL/6 mice and bisected sagitally. The anterior frontal cortex and olfactory bulb were dissected from each hemisphere and processed in the same manner as the neonatal samples.

Ice-cold radioimmunoprecipitation assay (RIPA) buffer (catalog number 89900; Thermo Fisher) containing 1% Halt protease inhibitor cocktail (catalog number 78430; Thermo Fisher) was added into the tissue collection tube at a ratio of 1:10 to the weight of the tissue sample. Samples were then mechanically lysed using the Benchmark Bead Bug tissue homogenizer (catalog number 1030) for 45 s at 2,800 vibrations per minute and then rocked on a tissue culture shaker for 30 min at 4°C.

Motor neurons were cultured for 2 weeks on 2% Matrigel in PDL-treated tissue culture dishes. Motor neurons and RD and HeLa cell cultures were lysed with ice-cold RIPA buffer containing 1% Halt protease inhibitor cocktail. The cells were scraped, and then the cell lysate was collected into centrifuge tubes and rocked on a tissue culture shaker for 30 min at 4°C.

For all samples, the cell debris was pelleted by centrifugation at 20,800 × *g* at 4°C for 20 min. The supernatant was collected, and the final protein concentration was determined using a bicinchoninic acid (BCA) assay (catalog number 23225; Thermo Fisher). Samples were mixed with 4× Laemmli buffer with β-mercaptoethanol (catalog number 1610747; Bio-Rad) and heated for 15 min at 65°C. Samples were loaded into a 7.5% mini-Protean precast gel (catalog number 4561023; Bio-Rad) and run at 150 V for 55 min in 1× Tris-glycine-SDS buffer (catalog number 1610732; Bio-Rad). The proteins were transferred onto polyvinylidene difluoride (PVDF) blots and blocked with 5% dry milk powder in 1% Tris-buffered saline–Tween 20 (TBST) for 2 h. After blocking, the blots were incubated in primary antibody in 5% dry milk in TBST overnight at 4°C. Following five washes in TBST, the blots were incubated in secondary antibody in 5% dry milk in TBST for 1 h. After five washes in TBST, the blots were developed using SuperSignal West Pico chemiluminescent substrate (catalog number 34580; Thermo Fisher) and imaged using a FluorochemQ MultiImage III workstation. Images were brightened linearly and equally using FluorochemQ image software. Primary antibodies and working concentrations were as follows: for human tissues and human cell lines, rabbit anti-ICAM-5 (1:1,000; catalog number 192415; Abcam); for mouse tissue, goat anti-ICAM-5 1:500 μg/ml (catalog number AF1173; R&D Systems); and for all tissue, rabbit anti-β-actin (1:1,000; catalog number 4970; Cell Signaling). The secondary antibodies used were as follows: horseradish peroxidase (HRP)-donkey anti-goat immunoglobulin (1:3,000; catalog number 705-035-003; Jackson Laboratories) and HRP-goat anti-rabbit immunoglobulin (1:3,000; catalog number 111-035-003; Jackson Laboratories).

RT-quantitative PCR (qPCR). Neonatal and adult mouse samples were collected as described above (see "Western blotting" above). Tissues were placed in Bead Bug tubes containing ice-cold RLT buffer (catalog number 79216; Qiagen) and 1% β-mercaptoethanol. The tissue was mechanically lysed in the collection tubes on a Bead Bug tissue homogenizer for 45 s at 2,800 vibrations per minute. RNA was purified from the lysate using a Qiagen RNeasy minikit (catalog number 74106) according to the manufacturer's instructions. Purified RNA was quantified using an AlphaSpec μL spectrophotometer. cDNA was prepared using a Bio-Rad iScript reverse transcription (RT) kit (catalog number 1708840) with 1 μg of purified RNA. cDNA was diluted in 400 μl of double-distilled H_2O, and then 2 μl was mixed with primers and amplified using a Bio-Rad 2× SYBR green kit (catalog number 1708880) in a 96-well plate in a Bio-Rad CFX96 thermocycler. Relative gene expression was normalized to that of β-actin. The following primers were obtained from Bio-Rad: mouse ICAM-5 (unique assay identifier, qMmuCED0004082), mouse β-actin (unique assay identifier, qMmuCED0027505).

Statistical analysis. Viral titers were $\log_{10}$ transformed, and statistical analysis was performed in GraphPad Prism (version 7) software. Titer values that fell below the limit of detection were set to the limit of detection. Axonal infection groups were compared using a one-way analysis of variance (ANOVA), followed by Tukey's multiple-comparison test. Mouse ICAM-5 CNS expression was compared using a one-way ANOVA, followed by Tukey's multiple-comparison tests. Neuraminidase treatment groups were compared to the controls using a Welch's *t* test.

ACKNOWLEDGMENTS

We thank David M. Brown, Richard H. Scheuermann, Mark Novotny, and Brian D. Aevermann at the J. Craig Venter Institute for information regarding the SH-SY5Y cell transcriptomics, as described in the Discussion. We thank Nicholas Baird and Christina Como from the University of Colorado for their advice on the technical aspects of neuron culture in microfluidic chambers. We thank Jeff Moore from the University of Colorado for donating the nocodazole and his expertise on axonal transport mechanisms. We thank Jeffrey Bennett and the Bennett lab at the University of Colorado for donating the NF antibody. We thank Mark Lovell at Children's Hospital Colorado and Michael Grainer and Anthony Fringuello at the University of Colorado Department of Neurology for help in obtaining the human tissue samples. We thank Gavin Ryan from Olympus for his assistance with the imaging methods.

We acknowledge support by grants R01 NS101208 (to K.L.T.) and F30 AI136403-01A1 (to A.M.H) from NIH.

REFERENCES

1. Pons-Salort M, Parker EP, Grassly NC. 2015. The epidemiology of non-polio enteroviruses: recent advances and outstanding questions. Curr Opin Infect Dis 28:479–487. https://doi.org/10.1097/QCO.0000000000000187.
2. Huang HI, Shih SR. 2015. Neurotropic enterovirus infections in the central nervous system. Viruses 7:6051–6066. https://doi.org/10.3390/v7112920.
3. Racaniello VR. 2006. One hundred years of poliovirus pathogenesis. Virology 344:9–16. https://doi.org/10.1016/j.virol.2005.09.015.
4. Rhoades RE, Tabor-Godwin JM, Tsueng G, Feuer R. 2011. Enterovirus infections of the central nervous system. Virology 411:288–305. https://doi.org/10.1016/j.virol.2010.12.014.
5. Messacar K, Abzug MJ, Dominguez SR. 2016. The emergence of enterovirus-D68. Microbiol Spectr 4:EI10-0018-2016. https://doi.org/10.1128/microbiolspec.EI10-0018-2016.
6. Messacar K, Asturias EJ, Hixon AM, Van Leer-Buter C, Niesters HGM, Tyler KL, Abzug MJ, Dominguez SR. 2018. Enterovirus D68 and acute flaccid myelitis—evaluating the evidence for causality. Lancet Infect Dis 18:e239–e247. https://doi.org/10.1016/S1473-3099(18)30094-X.
7. Maloney JA, Mirsky DM, Messacar K, Dominguez SR, Schreiner T, Stence NV. 2015. MRI findings in children with acute flaccid paralysis and cranial nerve dysfunction occurring during the 2014 enterovirus D68 outbreak. AJNR Am J Neuroradiol 36:245–250. https://doi.org/10.3174/ajnr.A4188.
8. Messacar K, Abzug MJ, Dominguez SR. 2016. 2014 outbreak of enterovirus D68 in North America. J Med Virol 88:739–745. https://doi.org/10.1002/jmv.24410.
9. Sejvar JJ, Lopez AS, Cortese MM, Leshem E, Pastula DM, Miller L, Glaser C, Kambhampati A, Shioda K, Aliabadi N, Fischer M, Gregoricus N, Lanciotti R, Nix WA, Sakthivel SK, Schmid DS, Seward JF, Tong S, Oberste MS, Pallansch M, Feikin D. 2016. Acute flaccid myelitis in the United States, August-December 2014: results of nationwide surveillance. Clin Infect Dis 63:737–745. https://doi.org/10.1093/cid/ciw372.
10. Hovden IA, Pfeiffer HC. 2015. Electrodiagnostic findings in acute flaccid myelitis related to enterovirus D68. Muscle Nerve 52:909–910. https://doi.org/10.1002/mus.24738.
11. Nathanson N, Langmuir AD. 1963. The Cutter Incident. Poliomyelitis following formaldehyde- inactivated poliovirus vaccination in the United States during the spring of 1955. I. Background. Am J Hyg 78:16–28.
12. Racaniello VR, Ren R. 1994. Transgenic mice and the pathogenesis of poliomyelitis. Arch Virol Suppl 9:79–86.
13. Gromeier M, Wimmer E. 1998. Mechanism of injury-provoked poliomyelitis. J Virol 72:5056–5060.
14. Li H, Su L, Zhang T, He F, Yin Y. 7 February 2019. MRI reveals segmental distribution of enterovirus lesions in the central nervous system: a probable clinical evidence of retrograde axonal transport of EV-A71. J Neurovirol https://doi.org/10.1007/s13365-019-00724-3.
15. Tan SH, Ong KC, Wong KT. 2014. Enterovirus 71 can directly infect the brainstem via cranial nerves and infection can be ameliorated by passive immunization. J Neuropathol Exp Neurol 73:999–1008. https://doi.org/10.1097/NEN.0000000000000122.
16. Chen CS, Yao YC, Lin SC, Lee YP, Wang YF, Wang JR, Liu CC, Lei HY, Yu CK. 2007. Retrograde axonal transport: a major transmission route of enterovirus 71 in mice. J Virol 81:8996–9003. https://doi.org/10.1128/JVI.00236-07.
17. Hixon AM, Yu G, Leser JS, Yagi S, Clarke P, Chiu CY, Tyler KL. 2017. A mouse model of paralytic myelitis caused by enterovirus D68. PLoS Pathog 13:e1006199. https://doi.org/10.1371/journal.ppat.1006199.
18. Hixon AM, Clarke P, Tyler KL. 2017. Evaluating treatment efficacy in a mouse model of enterovirus D68-associated paralytic myelitis. J Infect Dis 216:1245–1253. https://doi.org/10.1093/infdis/jix468.
19. Brown DM, Hixon AM, Oldfield LM, Zhang Y, Novotny M, Wang W, Das SR, Shabman RS, Tyler KL, Scheuermann RH. 2018. Contemporary circulating enterovirus D68 strains have acquired the capacity for viral entry and replication in human neuronal cells. mBio 9:e01954-18. https://doi.org/10.1128/mBio.01954-18.
20. Baggen J, Thibaut HJ, Staring J, Jae LT, Liu Y, Guo H, Slager JJ, de Bruin JW, van Vliet ALW, Blomen VA, Overduin P, Sheng J, de Haan CAM, de Haan Xander CAM, de Vries E, Meijer A, Rossmann MG, Brummelkamp TR, van Kuppeveld FJM. 2016. Enterovirus D68 receptor requirements unveiled by haploid genetics. Proc Natl Acad Sci U S A 113:1399–1404. https://doi.org/10.1073/pnas.1524498113.
21. Wei W, Guo H, Chang J, Yu Y, Liu G, Zhang N, Willard SH, Zheng S, Yu XF. 2016. ICAM-5/telencephalin is a functional entry receptor for enterovirus D68. Cell Host Microbe 20:631–641. https://doi.org/10.1016/j.chom.2016.09.013.
22. Taylor AM, Blurton-Jones M, Rhee SW, Cribbs DH, Cotman CW, Jeon NL. 2005. A microfluidic culture platform for CNS axonal injury, regeneration and transport. Nat Methods 2:599–605. https://doi.org/10.1038/nmeth777.
23. Park JW, Vahidi B, Taylor AM, Rhee SW, Jeon NL. 2006. Microfluidic culture platform for neuroscience research. Nat Protoc 1:2128–2136. https://doi.org/10.1038/nprot.2006.316.
24. Liu WW, Goodhouse J, Jeon NL, Enquist LW. 2008. A microfluidic chamber for analysis of neuron-to-cell spread and axonal transport of an alpha-herpesvirus. PLoS One 3:e2382. https://doi.org/10.1371/journal.pone.0002382.
25. Ohka S, Matsuda N, Tohyama K, Oda T, Morikawa M, Kuge S, Nomoto A. 2004. Receptor (CD155)-dependent endocytosis of poliovirus and retrograde axonal transport of the endosome. J Virol 78:7186–7198. https://doi.org/10.1128/JVI.78.13.7186-7198.2004.
26. Erturk A, Hellal F, Enes J, Bradke F. 2007. Disorganized microtubules underlie the formation of retraction bulbs and the failure of axonal regeneration. J Neurosci 27:9169–9180. https://doi.org/10.1523/JNEUROSCI.0612-07.2007.
27. Verstraelen P, Detrez JR, Verschuuren M, Kuijlaars J, Nuydens R, Timmermans JP, De Vos WH. 2017. Dysregulation of microtubule stability impairs morphofunctional connectivity in primary neuronal networks. Front Cell Neurosci 11:173. https://doi.org/10.3389/fncel.2017.00173.
28. Brandenburg B, Lee LY, Lakadamyali M, Rust MJ, Zhuang X, Hogle JM. 2007. Imaging poliovirus entry in live cells. PLoS Biol 5:e183. https://doi.org/10.1371/journal.pbio.0050183.
29. Liu Y, Sheng J, Baggen J, Meng G, Xiao C, Thibaut HJ, van Kuppeveld FJ, Rossmann MG. 2015. Sialic acid-dependent cell entry of human enterovirus D68. Nat Commun 6:8865. https://doi.org/10.1038/ncomms9865.
30. Gahmberg CG, Ning L, Paetau S. 2014. ICAM-5: a neuronal dendritic

adhesion molecule involved in immune and neuronal functions. Adv Neurobiol 8:117–132. https://doi.org/10.1007/978-1-4614-8090-7_6.
31. Yang H. 2012. Structure, expression, and function of ICAM-5. Comp Funct Genomics 2012:368938. https://doi.org/10.1155/2012/368938.
32. Yoshihara Y, Oka S, Nemoto Y, Watanabe Y, Nagata S, Kagamiyama H, Mori K. 1994. An ICAM-related neuronal glycoprotein, telencephalin, with brain segment-specific expression. Neuron 12:541–553. https://doi.org/10.1016/0896-6273(94)90211-9.
33. Tian L, Nyman H, Kilgannon P, Yoshihara Y, Mori K, Andersson LC, Kaukinen S, Rauvala H, Gallatin WM, Gahmberg CG. 2000. Intercellular adhesion molecule-5 induces dendritic outgrowth by homophilic adhesion. J Cell Biol 150:243–252. https://doi.org/10.1083/jcb.150.1.243.
34. Lindsberg PJ, Launes J, Tian L, Valimaa H, Subramanian V, Siren J, Hokkanen L, Hyypia T, Carpen O, Gahmberg CG. 2002. Release of soluble ICAM-5, a neuronal adhesion molecule, in acute encephalitis. Neurology 58:446–451. https://doi.org/10.1212/wnl.58.3.446.
35. Tse MC, Lane C, Mott K, Onlamoon N, Hsiao HM, Perng GC. 2009. ICAM-5 modulates cytokine/chemokine production in the CNS during the course of herpes simplex virus type 1 infection. J Neuroimmunol 213:12–19. https://doi.org/10.1016/j.jneuroim.2009.06.007.
36. Brown A. 2003. Axonal transport of membranous and nonmembranous cargoes: a unified perspective. J Cell Biol 160:817–821. https://doi.org/10.1083/jcb.200212017.
37. Maday S, Twelvetrees AE, Moughamian AJ, Holzbaur EL. 2014. Axonal transport: cargo-specific mechanisms of motility and regulation. Neuron 84:292–309. https://doi.org/10.1016/j.neuron.2014.10.019.
38. Mueller S, Cao X, Welker R, Wimmer E. 2002. Interaction of the poliovirus receptor CD155 with the dynein light chain Tctex-1 and its implication for poliovirus pathogenesis. J Biol Chem 277:7897–7904. https://doi.org/10.1074/jbc.M111937200.
39. Virgin HW, IV, Bassel-Duby R, Fields BN, Tyler KL. 1988. Antibody protects against lethal infection with the neurally spreading reovirus type 3 (Dearing). J Virol 62:4594–4604.
40. Clarke P, Leser JS, Bowen RA, Tyler KL. 2014. Virus-induced transcriptional changes in the brain include the differential expression of genes associated with interferon, apoptosis, interleukin 17 receptor A, and glutamate signaling as well as flavivirus-specific upregulation of tRNA synthetases. mBio 5:e00902-14. https://doi.org/10.1128/mBio.00902-14.
41. Zhang C, Zhang X, Dai W, Liu Q, Xiong P, Wang S, Geng L, Gong S, Huang Z. 2018. A mouse model of enterovirus D68 infection for assessment of the efficacy of inactivated vaccine. Viruses 10:E58. https://doi.org/10.3390/v10020058.
42. Sun S, Bian L, Gao F, Du R, Hu Y, Fu Y, Su Y, Wu X, Mao Q, Liang Z. 2019. A neonatal mouse model of enterovirus D68 infection induces both interstitial pneumonia and acute flaccid myelitis. Antiviral Res 161:108–115. https://doi.org/10.1016/j.antiviral.2018.11.013.
43. Arber S. 2012. Motor circuits in action: specification, connectivity, and function. Neuron 74:975–989. https://doi.org/10.1016/j.neuron.2012.05.011.
44. Daley JK, Gechman LA, Skipworth J, Rall GF. 2005. Poliovirus replication and spread in primary neuron cultures. Virology 340:10–20. https://doi.org/10.1016/j.virol.2005.05.032.
45. Griffin DE, Levine B, Ubol S, Hardwick JM. 1994. The effects of alphavirus infection on neurons. Ann Neurol 35(Suppl):S23–S27. https://doi.org/10.1002/ana.410350709.
46. Ahn J, Jee Y, Seo I, Yoon SY, Kim D, Kim YK, Lee H. 2008. Primary neurons become less susceptible to coxsackievirus B5 following maturation: the correlation with the decreased level of CAR expression on cell surface. J Med Virol 80:434–440. https://doi.org/10.1002/jmv.21100.
47. Midgley CM, Watson JT, Nix WA, Curns AT, Rogers SL, Brown BA, Conover C, Dominguez SR, Feikin DR, Gray S, Hassan F, Hoferka S, Jackson MA, Johnson D, Leshem E, Miller L, Nichols JB, Nyquist AC, Obringer E, Patel A, Patel M, Rha B, Schneider E, Schuster JE, Selvarangan R, Seward JF, Turabelidze G, Oberste MS, Pallansch MA, Gerber SI, EV-D68 Working Group. 2015. Severe respiratory illness associated with a nationwide outbreak of enterovirus D68 in the USA (2014): a descriptive epidemiological investigation. Lancet Respir Med 3:879–887. https://doi.org/10.1016/S2213-2600(15)00335-5.
48. Greninger AL, Naccache SN, Messacar K, Clayton A, Yu G, Somasekar S, Federman S, Stryke D, Anderson C, Yagi S, Messenger S, Wadford D, Xia D, Watt JP, Van Haren K, Dominguez SR, Glaser C, Aldrovandi G, Chiu CY. 2015. A novel outbreak enterovirus D68 strain associated with acute flaccid myelitis cases in the USA (2012–14): a retrospective cohort study. Lancet Infect Dis 15:671–682. https://doi.org/10.1016/S1473-3099(15)70093-9.
49. Zhang Y, Cao J, Zhang S, Lee AJ, Sun G, Larsen CN, Zhao H, Gu Z, He S, Klem EB, Scheuermann RH. 2016. Genetic changes found in a distinct clade of enterovirus D68 associated with paralysis during the 2014 outbreak. Virus Evol 2:vew015. https://doi.org/10.1093/ve/vew015.
50. Zheng Q, Zhu R, Xu L, He M, Yan X, Liu D, Yin Z, Wu Y, Li Y, Yang L, Hou W, Li S, Li Z, Chen Z, Li Z, Yu H, Gu Y, Zhang J, Baker TS, Zhou ZH, Graham BS, Cheng T, Li S, Xia N. 2019. Atomic structures of enterovirus D68 in complex with two monoclonal antibodies define distinct mechanisms of viral neutralization. Nat Microbiol 4:124–133. https://doi.org/10.1038/s41564-018-0275-7.
51. Baggen J, Thibaut HJ, Strating J, van Kuppeveld F. 2018. The life cycle of non-polio enteroviruses and how to target it. Nat Rev Microbiol 16:368–381. https://doi.org/10.1038/s41579-018-0005-4.
52. Sivaguru M, Kabir MM, Gartia MR, Biggs DSC, Sivaguru BS, Sivaguru VA, Fried GA, Liu GL, Sadayappan S, Toussaint KC, Jr. 2017. Application of an advanced maximum likelihood estimation restoration method for enhanced-resolution and contrast in second-harmonic generation microscopy. J Microsc 267:397–408. https://doi.org/10.1111/jmi.12579.
53. Schindelin J, Arganda-Carreras I, Frise E, Kaynig V, Longair M, Pietzsch T, Preibisch S, Rueden C, Saalfeld S, Schmid B, Tinevez JY, White DJ, Hartenstein V, Eliceiri K, Tomancak P, Cardona A. 2012. Fiji: an open-source platform for biological-image analysis. Nat Methods 9:676–682. https://doi.org/10.1038/nmeth.2019.